scientific reports

Check for updates

OPEN

Adaptive non unit traveling wave protection algorithm for multi terminal HVDC grids

Ali Raza[1], Muhammad Ameer Hamza[1], Abul Rehman Kashif[1], Muhammad Zain Yousaf[2,3]✉, Baseem Khan[3,5,6]✉, Josep M. Guerrero[2,3] & Rajkumar Sivanraju[4]✉

High Voltage Direct Current (HVDC) systems offer an efficient solution for long-distance power transmission and the integration of remote renewable energy sources. However, protection of the HVDC transmission line poses a significant challenge due to its extremely high short circuit currents and absence of zero crossings. DC faults must be resolved within milliseconds to prevent HVDC grid failure. Thus, advanced protection techniques are crucial for ensuring the efficiency and stability of multi-terminal Voltage Source Converter (VSC) based HVDC systems. This paper proposes a robust and adaptive non-unit protection algorithm for a multi-terminal HVDC grid transmission line, addressing DC fault type discrimination and fault identification under high-impedance fault (HIF) conditions. The algorithm is designed based on distinctive high-frequency components present in the line and pole mode voltage traveling waves (TWs) at various relay units. Daubechies wavelet transform was chosen as the time-frequency tool. The proposed protection scheme accurately detect fault and distinguishes between external and internal DC faults within one millisecond and ensures proper operation during HIF with a 25 dB level of noise interference. A four-terminal meshed HVDC grid is modeled in EMTDC/PSCAD and tested under the positive pole-to-ground (PTG), pole-to-pole (PTP), and negative pole-to-ground (NTG) fault at various locations and times to evaluate the effectiveness of the proposed protection scheme. By exploiting the properties of traveling waves, the algorithm improves the accuracy of DC fault protection, making it suitable for modern HVDC applications. The results indicate that the proposed protection algorithm offers enhanced sensitivity and improved selection performance.

Keywords DC grid protection, Daubechies wavelets transform, Multi-terminal high voltage direct current (MT-HVDC) grid, Non-unit protection, Traveling waves

Multi-terminal voltage source converter (VSC) based high voltage direct current (HVDC) grids are more reliable in transferring power from long-distance renewable energy sources like offshore wind farms, compared to AC transmission[1]. Several features of HVDC support its increasing integration into power systems, including (i) a significant decrease in transmission loss, (ii) the capability of transferring the power undersea or underground[2], (iii) reliable, cost-efficient, and safe solutions for future super grid (iv) enhance grid stability, (v) better voltage regulation and (vi) offer better control. However, the protection of HVDC systems continues to be a significant challenge. During a DC fault, the voltage undergoes a sharp decline, while the fault current rises abruptly to manifolds. These high currents can cause damage to converter stations and thus can lead to the failure of the entire system. Therefore, a reliable and fast protection algorithm is essential for HVDC systems to prevent adverse effects on system components. In recent years, several protection methods have been proposed. The existing traveling wave-based protection schemes are classified into two main types (i) unit method[3] and (ii) non-unit method[4].

The unit protection method depends on the communication channels to transmit data between the relays situated at both ends of the transmission line. The unit protection method detects faults within a defined zone or fixed boundary. Several unit-based protection approaches have been proposed for HVDC systems including

[1]Department of Electrical Engineering, University of Engineering & Technology, Lahore 54000, Pakistan. [2]School of Aeronautics and Astronautics, Zhejiang University, Hangzhou 310027, Zhejiang, China. [3]Huanjiang Laboratory, Center for Research on Microgrids (CROM), Zhuji, Shaoxing 311800, Zhejiang, China. [4]Department of Mechanical Engineering, Hawassa University, Hawassa, Ethiopia. [5] Department of Technical Sciences, Western Caspian University, Baku, Azerbaijan. [6] Electrical Engineering Department, Faculty of Engineering, University of Tabuk, Tabuk, Saudi Arabia. ✉email: mzainy1@gmail.com; baseem.khan04@gmail.com; rajkumar@hu.edu.et

voltage differential method[5], current differential[6], and impedance differential method[7]. The challenges and drawbacks associated with the unit protection method include difficulty in synchronizing data from multiple relays over a long transmission line, and fault detection delay due to communication channels. Moreover, unit protection methods have high implementation costs due to specialized communication channels and equipment needs[8]. Samwise due to data synchronization challenges; high maintenance costs, and fault detection delays, the unit protection method is not suitable for this study.

The non-unit-based protection method does not depend on communication channels, has no fixed boundary, and detects faults with local measurements. Non-unit protection methods include the (i) DC inductor voltage-based protection method[9], (ii) Time domain traveling wave-based protection method[10] or derivation-based protection method, and (iii) Time-frequency traveling wave protection method[11].

In the DC inductor voltage method, inductors are installed at each end of the transmission line. Fault detection is achieved by comparing the inductor voltage difference between negative and positive poles[12]. The DC inductor voltage method cannot identify high-impedance faults[13] and fails to detect PTG[14].

In the time domain traveling wave (TWs) method, the fault identification is based on the locally measured rate of the change of voltage (ROCOV) and rate of the change of current (ROCOC)[15]. The ROCOV and ROCOC are also called derivation-based protection methods[16]. ROCOV identifies faults by detecting sudden dip in system voltage[17], and in ROCOC, a fault is detected when the current surpasses a predefined threshold. The time domain TW technique may not detect high-impedance faults and may be sensitive to noise and cause false tripping. Fourier Transform (FT) and Fast Fourier Transform (FFT) are also used to detect faults in the frequency domain. The FT is not an appropriate technique to detect faults for transient signals because the time domain information is lost in the FT[18]. For exact fault detection of transient signals, time-frequency techniques are suitable as compared to the FT[19].

Several time-frequency methods, including Hilbert Huang Transformation (HHT)[20] and Short Time Fourier Transform (STFT)[21] have been used to detect faults in HVDC systems. The STFT partially solves the limitations of the standard Fourier transform. However, it does not provide clear time-frequency information. The performance of STFT is limited by a fixed window length[22]. The HHT is often sensitive to noise[23]. However, the resolution of HHTs is limited by the selection of intrinsic mode functions (IMF), which can reduce its suitability for industrial applications. The continuous wavelet transform overcomes the limitations of STFT by providing better resolution for high-frequency signals[24]. The continuous wavelet transform demands a very high sampling frequency (2 MHz) and additional synchronized devices. Similarly[25], used wavelets to extract transient signal frequency components. However, the protection schemes of CWT have limitations, including computational burden, high memory usage, and noise sensitivity.

The existing time-frequency methods such as STFT, HHT, and CWT often struggle with fixed window lengths, IMF dependence, and computational burden, respectively, which reduces the efficiency in DC fault detection. Additionally, identifying high fault resistance remains a major challenge due to lower fault currents. To enhance the robustness of fault detection in multi-terminal HVDC systems, this paper introduces a non-unit traveling wave-based protection algorithm. The fault identification and fault-pole selection are then developed based on Daubechies wavelet transform. Compared to traditional time-frequency approaches, the Daubechies wavelet transform provides better noise-filtering capabilities, low computational load, enabling accurate decomposition of signals into their detail (high frequency) and approximation (low frequency) components.

The structure of paper is outlined as follows. Section "Test system under study" presents the test system configuration and control strategies. Theoretical derivation of pole mode voltage traveling waves following a DC fault is described in section "Theoretical derivation of high-frequency elements in pole and line mode voltages". Section "Proposed protection scheme for multi-terminal VSC-HVDC systems" introduces the proposed protection algorithm for MT-HVDC systems. Section "Simulations and results" includes the simulation results of the proposed algorithm. Section "Analysis of proposed protection scheme in comparison with existing techniques" provides a comparison of the proposed protection algorithm with existing techniques. Finally, the conclusions are drawn in section "Conclusion".

Test system under study

To validate the efficacy of the proposed protection algorithm, a meshed four-terminal HVDC grid with a bipolar configuration is modeled and simulated in EMTDC/PSCAD, as shown in Fig. 1. The test system consists of two offshore converters connected to AC wind farms, which facilitate power transmission to onshore converters linked to the mainland AC grid. The VSC assisted resonant current (VARC) dc circuit breakers (DCCBs) are implemented in series with 50mH DC inductors at each cable terminal, to control the rate of rise of the DC fault current. The lengths of the cables L_{24}, L_{12}, L_{13}, L_{34}, and L_{14} are 150 km, 100 km, 200 km, 100 km, and 200 km respectively. At each end of the cable, relay units are installed, and each unit operates based on the protection algorithm outlined in section "Proposed protection scheme for multi-terminal VSC-HVDC systems". For accurate dynamic system behavior, the DC cable of the test system is modeled using a frequency-dependent phase model[26]. The parameters of test system are listed in Table 1.

Control strategies

Figure 2 illustrates the control strategy implemented at the converter stations. The three-phase currents (I_{abc}) and voltages (V_{abc}) from the AC system are transformed into the direct-axis (I_d, V_d) and quadrature-axis (I_q, V_q) components using the Park Transformation. The phase angle of the grid is determined using a phase-locked loop[27]. The control mechanism of Modular multi-level converter (MMC) consists of outer and inner current control layers. The outer control loops determine the reference currents in the d-q frame of reference for the current inner controller, while the inner current control provides the reference voltage for the open loop controller. The outer controllers of MMC-1 and MMC-2 are set to control DC voltage and reactive power to

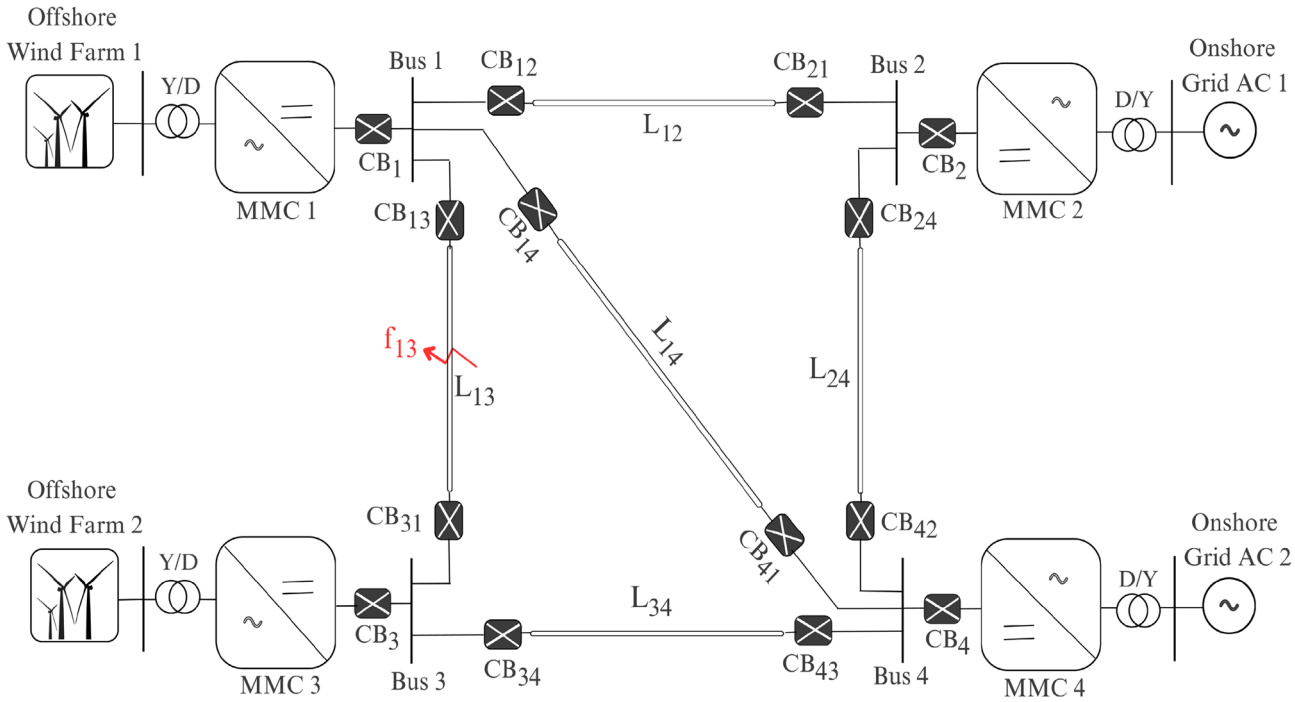

Fig. 1. MMC-HVDC grid test system.

System Parameters	Values
Converter topology	MMC
System frequency	50 Hz
MMC rated capacity	900 MVA
DC inductor	50 mH
Arm inductance L_{arm}	84 mH
Arm Resistance R_{arm}	0.08 Ω
Capacitance of SM C_{SM}	5 μF
Bus Filter Reactor	10 mH

Table 1. Test grid system parameters in PSCAD.

ensure stable power exchange with the offshore wind farms. Meanwhile, MMC-3 and MMC-4 regulate active and reactive power, ensuring a stable active power transfer and voltage stability at the onshore grid.

The outer control loop, including the DC voltage controller, reactive and active power controller, is represented by Eqs. (1)-(3), respectively.

$$I_d^{ref} = (V_{dc}^{ref} - V_{dc}^{meas})(k_p + \frac{k_i}{s}) \tag{1}$$

$$I_q^{ref} = (Q^{ref} - Q^{meas})(k_p + \frac{k_i}{s}) \tag{2}$$

$$I_d^{ref} = \frac{3}{2}(P^{ref} - P^{meas})(k_p + \frac{k_i}{s}) \tag{3}$$

The mathematical expression that defines the operation of the inner current controller is given as:

$$V_d^{ref} = V_d - \omega L I_q + k_p(I_d^{ref} - I_d) + k_i \int (I_d^{ref} - I_d) \tag{4}$$

$$V_q^{ref} = V_q + \omega L I_d + k_p(I_q^{ref} - I_q) + k_i \int (I_q^{ref} - I_q) \tag{5}$$

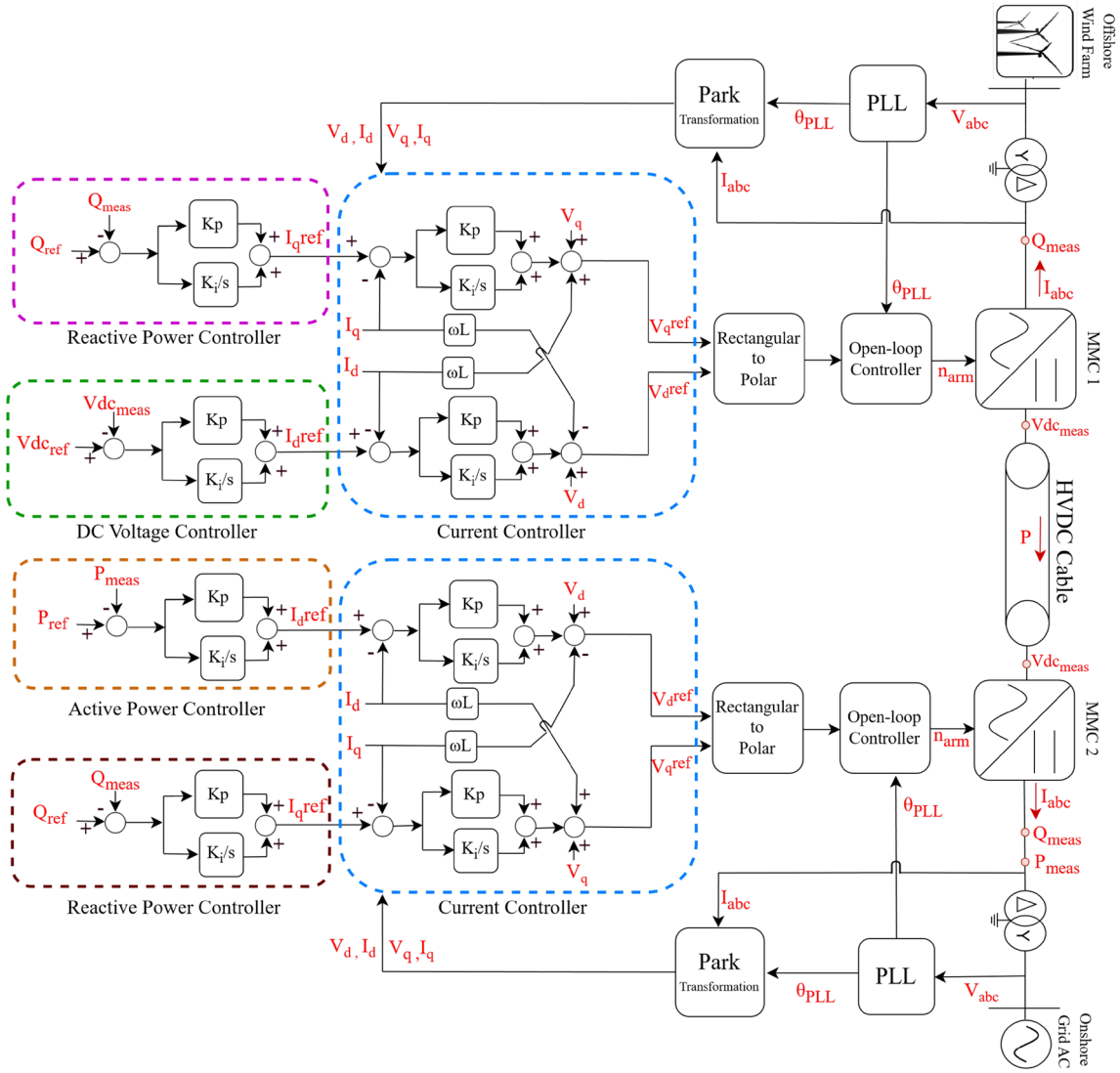

Fig. 2. Detailed control strategy applied to HVDC system.

Where V_d^{ref} and V_q^{ref} represent the reference voltages in the d-q frame of reference, which are transformed into polar coordinates. The resulting amplitude and phase are then fed into the open-loop controller[28] of the MMC, to determine the appropriate switching actions for each converter arm.

Protection zone layout

The HVDC system is divided into two protection zones: an internal protection (zone 1) and an external protection (zone 2). The internal zone covers the transmission line, while the external zone includes the DC bus. Each bus connects to multiple cables, with a breaker and relay at both ends as shown in Fig. 3. The Daubechies wavelet is used to differentiate between external and internal DC fault. When a fault occurs in a protection zone, only the breakers of that specific zone trip.

If the internal protection fails to act within the expected time, zone 2 relays act as a backup to isolate the fault. The relay coordination depends on a predefined time threshold to ensure proper action. Relay R_1 trips if $T_{R1}>T_{R13}+T_{CB13}$, pointing to a failure in internal protection.

Theoretical derivation of high-frequency elements in pole and line mode voltages

Initial voltage of line mode and zero mode components at fault location

In a bipolar DC system, the pole currents (i_P i_n) and voltages (V_P V_n) can be transformed into their corresponding zero modes (V_0, i_0) and line mode (V_1, i_1) components[29].

$$\begin{bmatrix} i_0 \\ i_1 \end{bmatrix} = \frac{1}{\sqrt{2}} \begin{bmatrix} 1 & 1 \\ 1 & -1 \end{bmatrix} \begin{bmatrix} i_P \\ i_n \end{bmatrix}, \quad \begin{bmatrix} V_0 \\ V_1 \end{bmatrix} = \frac{1}{\sqrt{2}} \begin{bmatrix} 1 & 1 \\ 1 & -1 \end{bmatrix} \begin{bmatrix} V_P \\ V_n \end{bmatrix} \tag{6}$$

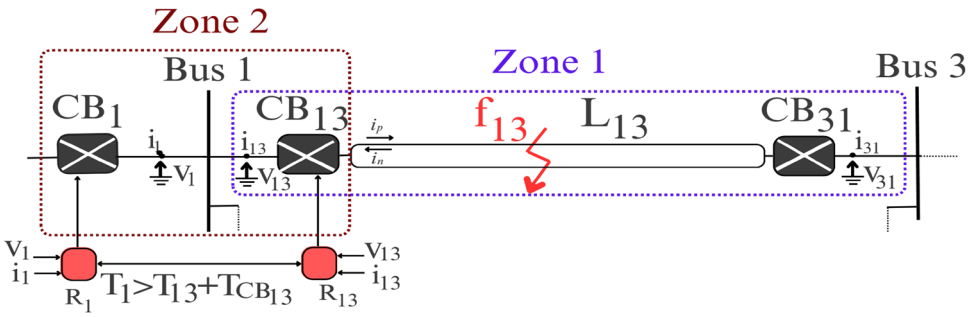

Fig. 3. Layout of protection zone for HVDC system.

Where i_p and i_n denote the currents in the positive and negative pole conductors, corresponding to their respective voltages V_p and V_n respectively. In Eq. (6), i_0 denotes the zero mode current, which returns through the ground during an unbalanced condition, while i_1 indicates the circulating current between the positive and negative poles. Similarly, V_0 and V_1 represent the zero mode and line mode voltages, respectively. By integrating the zero mode and line mode networks, fault parameters can be effectively analyzed for various fault types.

In a bipolar HVDC grid, when a fault occurs on the positive pole to ground, the corresponding fault-superimposed network, satisfies the following boundary conditions:

$$\begin{cases} V_P = V_a - 2i_P R_f \\ V_a = -V_{dc} \\ i_n = 0 \end{cases} \tag{7}$$

Where i_n =0 since, in the fault-superimposed network, the negative pole is not part of the fault return path in a PTG fault and hence has no incremental current. R_f represents fault resistance, and V_a is the voltage source representing the fault's influence. By enforcing the boundary conditions $i_n = 0$, $V_0 = i_0 Z_0$, and $V_1 = i_1 Z_1$ in Eq. (6), initial voltage traveling waves for both poles can be derived as:

$$\begin{cases} V_P = \dfrac{1}{\sqrt{2}}(Z_1 + Z_0) i_1 \\ V_n = \dfrac{1}{\sqrt{2}}(Z_0 - Z_1) i_0 \end{cases} \tag{8}$$

Where Z_0 and Z_1 are the zero-mode and line-mode wave impedance, respectively.

By merging (7) and (8), the zero and the line mode current can be expressed as:

$$\begin{cases} i_0 = \dfrac{-V_{dc}\sqrt{2}}{Z_0 + Z_1 + 4R_f} \\ i_1 = \dfrac{-V_{dc}\sqrt{2}}{Z_1 + Z_0 + 4R_f} \end{cases} \tag{9}$$

According to the impedance relationship, the zero mode and line mode currents in (9) are defined by their respective voltages, with the initial voltage-traveling wave for the PTG fault given as:

$$\begin{cases} V_0 = \dfrac{-\sqrt{2}V_{dc}Z_0}{Z_1 + Z_0 + 4R_f} \\ V_1 = \dfrac{-\sqrt{2}V_{dc}Z_1}{Z_1 + Z_0 + 4R_f} \end{cases} \tag{10}$$

In a similar manner, when NTG fault occurs, the corresponding voltage traveling waves can expressed as:

$$\begin{cases} V_0 = \dfrac{\sqrt{2}V_{dc}Z_0}{Z_1 + Z_0 + 4R_f} \\ V_1 = \dfrac{-\sqrt{2}V_{dc}Z_1}{Z_1 + Z_0 + 4R_f} \end{cases} \tag{11}$$

Similarly, for a PTP fault, the voltage TW can be:

$$\begin{cases} V_0 = 0 \\ V_1 = \dfrac{-\sqrt{2}V_{dc}Z_1}{R_f + Z_1} \end{cases} \tag{12}$$

The line mode components focus on the propagation properties of traveling waves for two reasons. First, as indicated in (12), the zero-mode components are zero during PTP faults, causing the identification of PTP faults to become ineffective. Second, the line-mode components, as represented in (10) and (11), exhibit higher propagation velocities and lower attenuation constants compared to the zero-mode component, making them more effective for analyzing the behavior of the traveling wave in fault detection.

Formulation of line and zero mode voltage at internal relay

In this case, Cable 13 in Fig. 1 is considered as the faulted cable. For fault f_{13}, the line-mode fault components were analyzed using the Petersen equivalent circuit in both the time and S-domains, as shown in Fig. 4. In Fig. 4(a), the voltage at the fault inception point is twice the initial voltage due to the reflected and incident traveling waves in the faulty cable. Z_{Conv} denotes the converter equivalent impedance, typically formulated as a series RLC circuit:

$$C_{eq} = \frac{6C_{SM}}{N}\ ,\quad R_{eq} = \frac{2(R_{on} + R_{arm})}{3}\ ,\quad L_{eq} = \frac{2L_{arm}}{3} \tag{13}$$

In (13), C_{eq}, L_{eq}, and R_{eq} denote the equivalent capacitance, inductance, and resistance of the converter, respectively. Whereas N specifies the total number of submodules, and R_{on} corresponds to the on-state resistance of the switches. In this test system, $R_{eq} = 0.057\Omega$, $C_{eq} = 15$uF, and $L_{eq} = 56$ mH.

Applying the Laplace transform, the impedance of the MMC is mathematically expressed as $Z_{Conv} = sL_{eq} + 1/sC_{eq}$, where the impact of the equivalent resistance is neglected due to its minimal effect compared to the dominant reactive components.

The impedance from Bus-1 to the MMC is $Z_p = Z_1 + sL_{dc}$. Therefore, the equivalent impedance Z_{b1} at Bus-1 can be defined as:

$$Z_{b1} = \frac{(sL_{eq} + \frac{1}{sC_{eq}})(Z_1 + sL_{dc})}{Z_1 + sL_{dc} + sL_{eq} + \frac{1}{sC_{eq}}} \tag{14}$$

According to Fig. 4(b), all components are connected in series, and the total impedance is the sum of the relay impedance Z_1, transmission line inductance sL_{dc}, and the bus impedance Z_{b1}. The line-mode voltage at the relay, $V_{(1)13}(s)$, in the S-domain can be calculated using voltage divider as follows:

$$V_{(1)13}(s) = \left(\frac{Z_1}{Z_1 + sL_{dc} + Z_{b1}}\right)\frac{2V_{F1}}{s} \tag{15}$$

As illustrated in Fig. 5, when a fault occurs at f_{13}, the backward traveling wave $V_{bw}(x, s)$ originates from the fault point and travels toward terminal B. In the initial phase, the backward traveling wave detected at terminal B in the S-domain is mathematically defined as:

$$V_{bw}(0, s) = e^{-\Upsilon_1(s)x}V_{bw}(x, s) \tag{16}$$

The term $e^{-\Upsilon_1(s)x}$ represents the propagation coefficient of the traveling wave. It can be denoted as[29]:

$$e^{-\Upsilon_1(s)x} \approx \frac{1 - k_1 x}{1 + sT_1 x}e^{\frac{-sx}{V_1}} \tag{17}$$

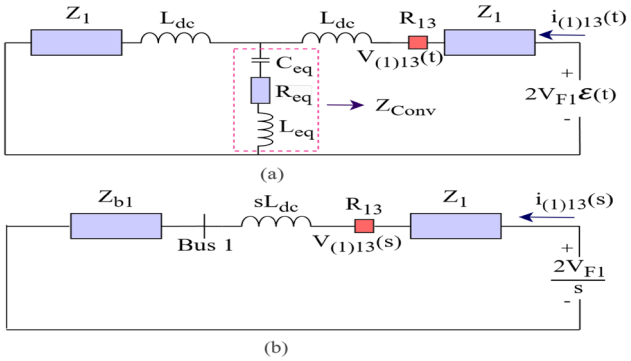

Fig. 4. (a): Peterson model representation in time domain (b): S-domain simplified circuit model.

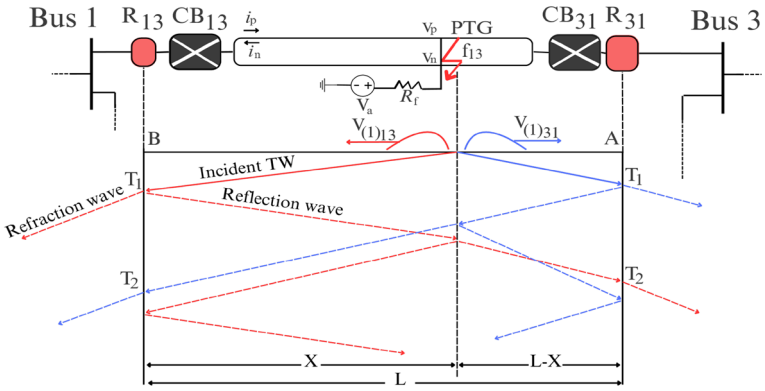

Fig. 5. Lattice diagram for PTG fault in line mode network.

Where $e^{-sx/v}$ describes the phase-change behavior of traveling waves in the line mode component. V_1 represents the propagation speed of line-mode traveling waves in the transmission line. T_1 is the time constant, representing the distortion of the traveling wave during its propagation. X represents the distance between fault f_{13} and terminal B. k_1 donates the attenuation coefficient, representing the impact of line-to-ground conductance and line resistance on the attenuation of traveling waves.

$$k_1 = \sqrt{(j\omega C_0 + g_0)(j\omega L_0 + r_0)} \tag{18}$$

Where C_0 and g_0 denote the per-unit line to ground capacitance and conductance, while L_0 and r_0 represent the per-unit inductance, and resistance in the distributed-parameter DC line model. Thus, the expression for $\mathbf{V}_{(1)13}(\mathbf{s})$ in (15), incorporating the fault distance x, given by:

$$V_{(1)13}(s) = \frac{2V_{F1}}{s}\left(\frac{Z_1}{Z_1 + sL_{dc} + Z_{b1}}\right)\frac{1 - k_1 x}{1 + sT_1 x}e^{\frac{-sx}{V_1}} \tag{19}$$

Due to the symmetrical properties of the system, the equation for $\mathbf{V}_{(1)13}(\mathbf{s})$ observed at relay R_{31} can be derived by substituting (L − x) for x in (19):

$$V_{(1)13}(s) = \frac{2V_{F1}}{s}\left(\frac{Z_1}{Z_1 + sL_{dc} + Z_{b1}}\right)\frac{1 - k_1(L - x)}{1 + sT_1(L - x)}e^{\frac{-(L-x)s}{V_1}} \tag{20}$$

Equations (19) and (20) highlight the attenuation effect of traveling waves over the distance as they propagate along the cable. The amplitude of the traveling wave decreases exponentially with distance due to the inherent resistive and inductive properties of the line.

Following (19), the zero-mode voltage $\mathbf{V}_{(0)13}(\mathbf{s})$, incorporating the fault distance x, given by:

$$V_{(0)13}(s) = \frac{2V_{F0}}{s}\left(\frac{Z_0}{Z_0 + sL_{dc} + Z_{b1}}\right)\frac{1 - k_0 x}{1 + sT_0 x}e^{\frac{-sx}{V_0}} \tag{21}$$

Where V_0 denotes the propagation characteristics of zero-mode traveling waves along the cable. The parameters k_0, and T_0 describe the characteristics of zero-mode traveling waves, with lower velocity and higher attenuation constant.

Formulation of line mode voltage components at external relay

A portion of the traveling wave initiated by fault point f_{13} propagates into the adjacent cable. Consequently, the voltage $\mathbf{V}_{(1)12}(\mathbf{s})$ measured at R_{12} is determined as:

$$V_{(1)12}(s) = \left(\frac{Z_1}{Z_1 + sL_{dc}}\right)\left(\frac{2V_{F1}}{s} - (Z_1 + sL_{dc})i_{(1)13}(s)\right) \tag{22}$$

Based on Fig. 5, $i_{(1)13}(s)$ can be calculated as:

$$i_{(1)13}(s) = \frac{2V_{F1}}{s}\left(\frac{1}{Z_1 + sL_{dc}}\right)\frac{1 - k_1 x}{1 + sT_1 x}e^{\frac{-sx}{V_1}} \tag{23}$$

Substituting (23) into (22) yields the following expression:

$$V_{(1)12}(s) = \left(\frac{Z_1}{Z_1 + sL_{dc}}\right)\left(\frac{2V_{F1}}{s} - \frac{2V_{F1}}{s}\frac{1 - k_1 x}{1 + sT_1 x}e^{\frac{-sx}{V_1}}\right) = \frac{2V_{F1}}{s}\left(1 - \frac{1 - k_1 x}{1 + sT_1 x}e^{\frac{-sx}{V_1}}\right)\left(\frac{Z_1}{Z_1 + sL_{dc}}\right) \quad (24)$$

The derived expression in (24) represents the traveling wave voltage at the external relay, incorporating the effects of impedance and transient propagation.

High-frequency voltage components in the faulted pole

By applying the inverse transformation of (6), the pole voltages at the fault point are:

$$V_{P13} = \frac{V_{(0)13} + V_{(1)13}}{\sqrt{2}}, \quad V_{n13} = \frac{V_{(0)13} - V_{(1)13}}{\sqrt{2}} \quad (25)$$

By combining Eqs. (19), (21), and (25), the derived expression is as follows:

$$V_{P13} = \frac{1}{\sqrt{2}}(A + B), \quad V_{n13} = \frac{1}{\sqrt{2}}(A - B) \quad (26)$$

The parameters in (26) are determined as follows:

$$\begin{cases} A = \dfrac{2Z_0 V_{F0}}{s(Z_0 + sL_{dc} + Z_{b1})}\dfrac{1 - k_0 x}{1 + sT_0 x}e^{\frac{-sx}{V_0}} \\ B = \dfrac{2Z_1 V_{F1}}{s(Z_1 + sL_{dc} + Z_{b1})}\dfrac{1 - k_1 x}{1 + sT_1 x}e^{\frac{-sx}{V_1}} \end{cases}$$

As stated in (12), V_0 is zero under PTP fault at fault point F. Since V_{F0} is zero in (26). As a result: $V_{P13}(s) = V_{n13}(s) = 1/\sqrt{2}\ V_{(1)13}(s)$. Upon the arrival of traveling waves at R_{13}, the pole voltages decrease rapidly, exhibiting symmetrical transients. In the case of NTG or PTG faults, only the voltage of the faulty pole will rapidly drop to zero, while the healthy pole undergoes slight damping. If the attenuation effect of traveling waves in (26) is neglected, the expression can be formulated as follows:

$$\lim_{s\to\infty}\left|\frac{V_{p13}(s)}{V_{n13}(s)}\right| = \begin{cases} \dfrac{Z_0 + Z_1}{Z_0 - Z_1}, & \text{PTG fault} \\ 1, & \text{PTP fault} \\ \dfrac{Z_0 - Z_1}{Z_0 + Z_1}, & \text{NTG fault} \end{cases} \quad (27)$$

As given in (27), the magnitude of $\frac{V_{p13}(s)}{V_{n13}(s)}$ varies with fault type as s→∞. The faulty pole voltages contain high-frequency components with larger amplitude compared to healthy poles. The fault region can be distinguished through the high-frequency components in the line voltages, whereas the fault type can be determined by analyzing the high frequency components in the pole mode voltages.

Proposed protection scheme for multi-terminal VSC-HVDC systems

This section presents the proposed protection scheme and its operational principles. It also explains the systematic approach used to select threshold values for accurate and reliable fault area detection and fault type identification.

Protection startup criteria

When a fault occurs, the DC voltage drops instantly. Therefore, protection startup criteria are determined based on DC voltage detection, expressed as:

$$|V_{p,ij} - V_{n,ij}| = |V_{dc,ij}| < V_{dc,Thr} \quad (28)$$

Where $V_{dc,Thr}$ represents the threshold for initiating the protection startup criterion. The selection of $V_{dc,Thr}$ requires a balance between sensitivity against high impedance fault (HIF) and robustness to noise interference. A threshold above 0.95 p.u. (305.54 kV) may lead to false activation under 25 dB Gaussian white noise, while a lower threshold may fail to detect HIFs. Simulation studies confirm that selecting $V_{dc,Thr}$ as 0.95 p.u. (305.54 kV) enables robust protection activation for internal high impedance fault (HIF), even under 25 dB noise interference.

Criterion for identifying fault area

The criterion of fault area identification relies on the maximum value of high-frequency components present in the line mode voltage. In this study, the Daubechies mother wavelet is chosen as the signal-processing technique primarily for its high accuracy, effective data compression, and computational efficiency[30]. For discrete signals, the Daubechies wavelet transform is expressed as:

$$DWT(f,p,q) = \frac{1}{\sqrt{a_0^p}} \sum_k f(k) \Psi^* \left(\frac{q - kb_0 a_0^p}{a_0^p} \right) \tag{29}$$

Where $a_0{}^p$ represents the scaling factor and $kb_0a_0{}^p$ represents the translating parameter.

The Daubechies discrete wavelet transform decomposes the signal f(k) into approximate (A_1 to A_4) as well as detailed (D_1 to D_4) coefficients using cascaded low and high pass filters. The detailed coefficients capture high-frequency components, while the approximate coefficients retain low-frequency components. The detailed and approximate coefficients are then down-sampled by a factor of two, enhancing frequency resolution while preserving time localization at each scale. The implementation of DWT was performed using the Dyadic Mallet Tree (DMT) algorithm, as depicted in Fig. 6.

The proposed algorithm employs fourth-level detailed coefficients for fault detection. Lower levels (such as 1st, 2nd, and 3rd) demand higher sampling frequency and are more sensitive to noise, while higher levels (such as 5th, 6th, and 7th) fail to accurately represent the traveling wave arrival time.

In this study, the DWT operates at a sampling frequency of 50 kHz to minimize delay, optimize resolution, and enhance protection performance. The criterion for identifying the fault area is determined as follows:

$$|d_4u_{(1)\,ij}| > d_4u_{(1)\,,Thr} \tag{30}$$

Where $d_4u_{(1)_{ij}}$ is the high-frequency wavelet coefficient of the line-mode signal at the fourth decomposition level, while $d_4u_{(1)_{ij,\ Thr}}$ represents the threshold used for fault area detection. The threshold value of fault area detection is determined using the following expression:

$$d_4u_{(1)\,,Thr} = \frac{median(|C_d|)}{0.6745} \sqrt{2\log(M)} \tag{31}$$

Where M is the length of the detailed coefficient, C_d donated the detailed coefficient.

Fault location based on injected traveling wave

When a fault occurs, a sudden change in impedance generates transient waves that propagate toward both terminals of the DC cable, as illustrated in Fig. 5. These waves undergo multiple reflections, affecting fault detection and location analysis. In this study, the arrival time of traveling waves is determined by analyzing the high-frequency wavelet coefficients ($d_4u_{(1)_{ij}}$). The arrival time corresponds to the first time index at which the absolute value of $d_4u_{(1)_{ij}}$ exceeds the threshold, defined in Eq. (30). The propagation time of reflected waves is used to determine the fault location from the point of measurement. Once the arrival times t_A and t_B at terminals A and B are detected, fault distance is determined using the following:

$$X_F = 0.5[L + (t_B - t_A)v] \tag{32}$$

Where L denotes the length of DC cable, t_B and t_A represent the arrival times of the traveling wave at points B and A respectively, and v indicates the speed at which the traveling wave propagates.

Criterion for identifying fault type

To identify the type of fault, the difference of wavelet energy ΔE_{ij} between negative and positive poles is calculated as follows:

$$\Delta E_{ij} = |Ed_4V_{p,ij}| - |Ed_4V_{n,ij}| \tag{33}$$

Here, $Ed_4u_{n,ij}$ and $Ed_4u_{p,ij}$ represent the wavelet energy associated with the negative and positive pole voltage in cable ij, calculated as:

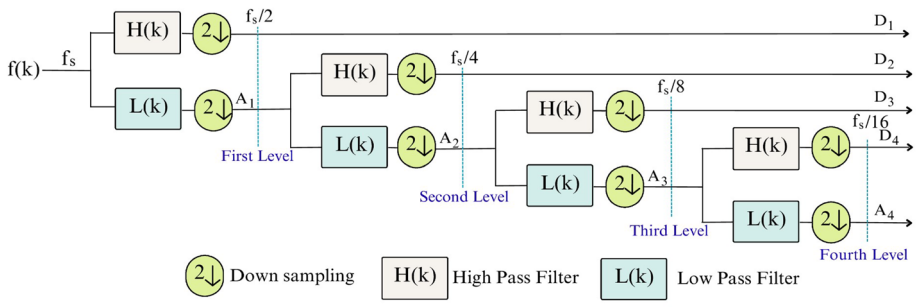

Fig. 6. Dyadic Mallet tree structure for DWT decomposition.

$$Ed_4V_{p,ij} = \sum_{k=1}^{\infty} [d_4u_{p,ij}(k)]^2$$

$$Ed_4V_{n,ij} = \sum_{k=1}^{\infty} [d_4u_{n,ij}(k)]^2$$

Where k denotes the time index of the wavelet coefficients at a specific decomposition level. Thus, the criterion for fault type identification is defined as follows:

$$\begin{cases} \Delta E_{ij} \leqslant \Delta E_1, & N\text{TG fault} \\ \Delta E_{ij} \geqslant \Delta E_2, & \text{PTG fault} \\ \Delta E_1 \leqslant \Delta E_{ij} \leqslant \Delta E_2, & P\text{TP fault} \end{cases} \tag{34}$$

Where ΔE_1 and ΔE_2 are fault identification thresholds. Due to system symmetry, ΔE_{ij} has equal magnitude but opposite polarity in NTG and PTG faults. Thus, ΔE_1 is expressed as $-\Delta E_2$.

Sequence of proposed protection scheme

The flowchart of the proposed algorithm is presented in Fig. 7, includes four steps. The voltage $V_{dc,ij}$ is initially tested to check whether start-up conditions are satisfied or not. If start-up conditions are satisfied, the algorithm proceeds to the next step, which identify the fault area as defined in (30). After identifying an internal fault, locate the fault position using the injected traveling wave, as described in (32). After that, the system performs fault type identification as explained in (34). Once the fault type is classified, the trip signal is issued to the corresponding VARC DCCB to interrupt the fault current; otherwise, the protection will reset.

For practical implementation, the proposed fault detection algorithm can be programmed in Field Programmable Gate Array (FPGA), a reconfigurable hardware device designed to perform parallel processing with high efficiency[31]. FPGA platforms, such as Altera Quartus and Xilinx Virtex, provide the computational power and flexibility to implement complex algorithms like the DWT using VHDL language (Very High-Speed Integrated Circuit Hardware Description Language). To meet the specified requirements, the design can be validated through a hardware-in-the-loop (HIL) setup with a Real-Time Digital Simulator (RTDS), ensuring rapid and accurate fault detection in real time. The communication between system components can be achieved via the Aurora protocol for high speed data transfer and the IEC 61850-9-2 standard[32]. Furthermore, DWT decomposition remains reliable under HIF conditions by capturing transient and non-stationary features at low fault currents, making it suitable for FPGA and DSP based protection schemes.

Simulations and results

All test faults occurred at 0.6s on cable 13 at different fault distances. The fault resistance varied from 0 to 500 Ω. A 50 kHz sampling rate was used in EMTDC/PSCAD to capture high-frequency components, which were analyzed using the Daubechies wavelet transform.

Protection performance under internal fault conditions

The start-up protection criteria for f_{13}|PTG (d = 25 km) and f_{13}|PTP (d = 100 km) is illustrates Fig. 8. When the voltage traveling waves reach relay R_{13}, the voltage $V_{dc,13}$ drops within 0.2ms. Fault resistance influences the start-up criteria, which affects the propagation of traveling waves along the faulty cable. The protection start-up threshold is 305.54 kV (0.95p.u.) and it is satisfied for fault resistances up to 500Ω, ensuring the necessary sensitivity to high-impedance faults.

Figure 9 illustrates the appearance of the detailed components of the wavelet coefficient under various fault conditions. Figure 9a and b depict PTG faults, whereas Fig. 9c and d show NTG faults, both at 25 km with fault resistances of 0Ω and 5Ω, respectively. Figure 9e and f present PTP faults at 100 km with fault resistances of 50Ω and 100Ω, respectively. Under pre-fault conditions, the amplitudes of $d_4u_{(1)13}$ are close to zero. When a fault occurs at 0.6s, oscillations and attenuation occur in the initial post-fault stage, along with the reflection and incident of the line-mode traveling wave. The magnitude of oscillations and attenuation depends on fault resistance and specific fault distance. At lower fault resistance, signals exhibit higher oscillation, making the transients more prominent. In contrast, higher fault resistance results in reduced oscillation amplitude. The maximum transient values are determined when line mode traveling waves reach the relay unit.

The difference in energy levels observed at relay R_{13} for fault events f_{13}|PTP (d = 25 km), f_{13}|PTG (d = 25 km), and f_{13}|NTG (d = 25 km), considering fault resistance values of 100Ω and 500Ω are illustrates in Fig. 10. Figure 10(a) and 10(b) show that when the traveling waves reach the cable endpoints, the wavelet energy of negative and positive poles rapidly increases to a distinguishable level. Due to the symmetrical transient response in a PTP fault, the wavelet energy at both poles is nearly identical, resulting in an energy difference close to zero. Figure 10(c) and (d) show the wavelet energy in the PTG fault. In this case, the positive pole has higher energy than the negative pole. Correspondingly, Fig. 10(e) and (f) depict the NTG fault, where the negative pole has higher wavelet energy than the positive pole. This feature helps in identifying the fault type using (34).

Tables 2 and 3, and 4 summarize the results obtained under PTG, NTG, and PTP fault for varying resistance values. For PTG faults, Table 2 shows that the $d_4u_{(1)13}$ value is significantly high at low resistance values and gradually decreases as the resistance increases. At low resistance values, $d_4u_{(1)13}$ values are high, indicating a strong transient response. Similarly, the wavelet energy ΔE_{13} shows a decreasing trend with increasing fault resistance, affecting the trip decision time. This shows that PTG faults are easier to detect at lower resistance values, with higher energy variations leading to faster trip decisions.

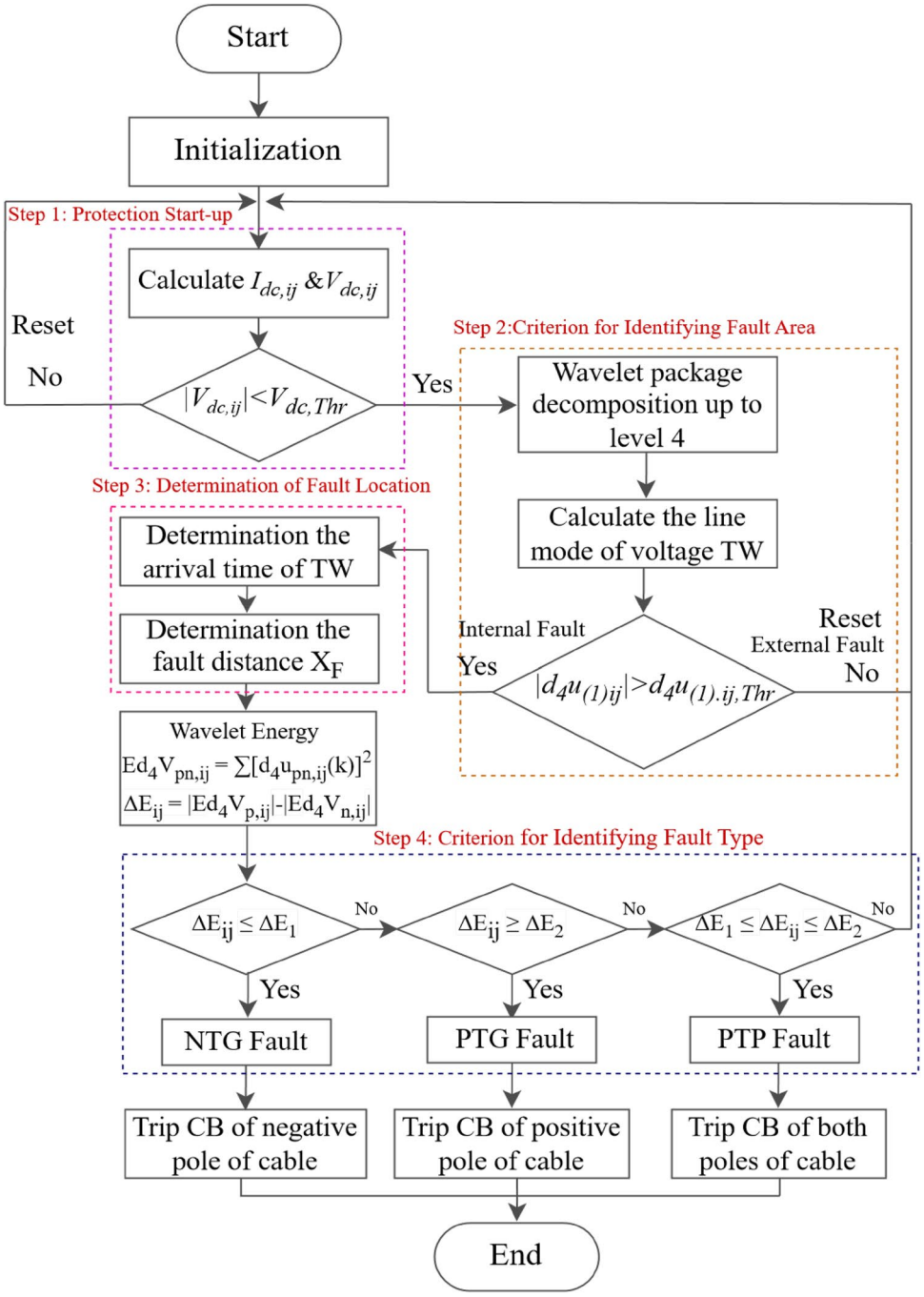

Fig. 7. Flowchart of proposed protection scheme.

For NTG faults, Table 3 shows that the trend in $d_4u_{(1)13}$ is similar to that of PTG faults but with negative voltage variations. The wavelet energy is also negative, shows a distinct wavelet characteristic for NTG faults, and confirming the protection scheme successfully identifies NTG faults with similar sensitivity.

For PTP faults, Table 4 detects a fault at a greater distance of 100 km. The value of $d_4u_{(1)13}$ is greater than NTG and PTG faults at 25 km. The difference in wavelet energy ΔE13 is approximately zero.

Overall, the results show that the Daubechies wavelet effectively detects faults across various fault resistances and types. Lower fault resistances result in greater voltage and energy variations, leading to faster trip responses.

Fault current interruption using VARC DCCBs

Figure 11 shows fault current interruption by the DCCB for a PTG fault at 25 km and PTP fault at 100 km with fault resistances of 0 Ω and 5 Ω respectively. In this scenario, the peak fault current is 3.98 kA at 0.608 s for a 0 Ω resistance at a distance of 25 km and 5.52 kA at 0.6091 s for a 5 Ω fault resistance at a distance of 100 km. The DCCB tripped after 0.61ms for the PTG fault and 0.63ms for the PTP fault, respectively. The sharp drop in

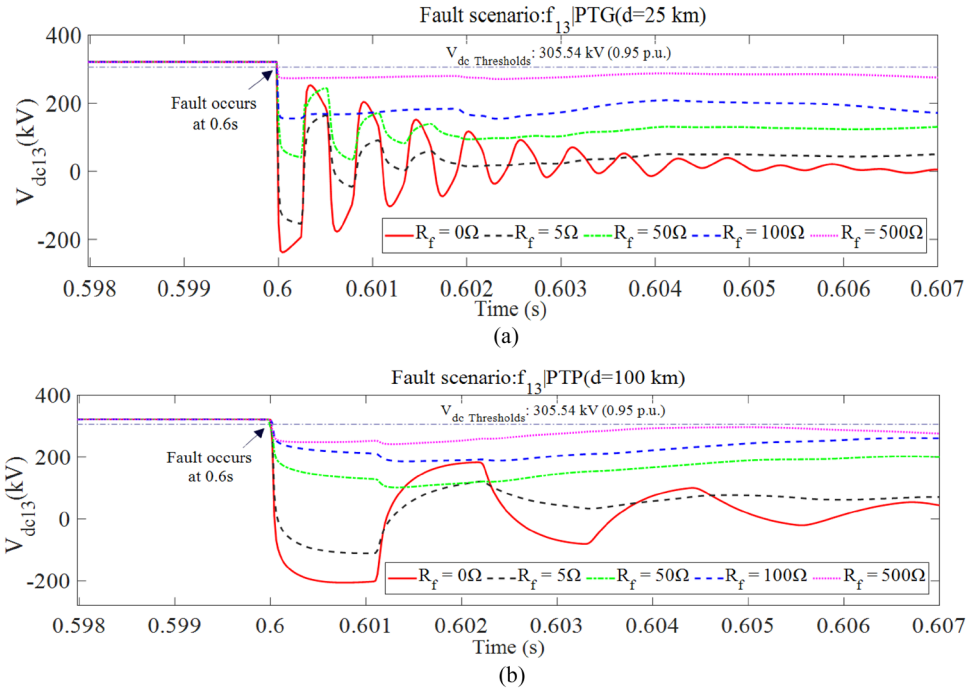

Fig. 8. Simulation results of $V_{dc,13}$ (a) f_{13}|PTG (d = 25 km). (b) f_{13}|PTP (d = 100 km).

current indicated that the proposed protection scheme works correctly by quickly stopping the fault current. The obtained results show that the proposed protection algorithm and the DCCBs exhibit effective interaction to interrupt fault current.

Protection performance during external fault conditions

Different external fault conditions were tested on the external zones of cable. Table 5 summarizes the detailed results obtained under external fault conditions. The maximum value of $d_4u_{(1)13}$ is 3.98 kV. Compared to the internal DC fault results in Tables 2 and 3, and 4, the magnitudes of $d_4u_{(1)13}$ are significantly smaller. The protection system resets, as shown in Fig. 6, Step 2, as external faults do not trigger detection.

When a fault occurs, the protection system of the affected cable operates, while the protections of non-faulted cable remain inactive due to the magnitudes of $d_4u_{(1)13}$ are significantly smaller. Table 6 presents the effect of a faulted cable on adjacent non-faulted cables.

Noise influence on purposed protection performance

Gaussian noise is introduced into the signals at different signal-to-noise ratios (25dB, 75dB, and 50dB) to evaluate the performance of the protection algorithm under noisy conditions. The studied system undergoes two independent fault scenarios, and the results for relay unit R_{13} are provided in Table 7. At a low signal-to-noise ratio (i.e., 25 dB), the system experiences higher noise levels. However, fault detection remains effective at lower fault resistances. At high signal-to-noise (e.g., 75 dB), the effect of noise is reduced, leading to improved signal accuracy. However, as fault resistance increases, fault identification becomes more challenging. The results validate that the protection algorithm is strong enough to handle noise interference up to 25 dB.

Analysis of proposed protection scheme in comparison with existing techniques

Table 8 presents a comparative analysis of the proposed algorithm against several well-established method from literature review including S-Transform[33], Hilbert-Huang Transform[34,35], Modal Domain Analysis[36], Discrete Wavelet Transform[37,38], and Fast Fourier Transform[39].

The method in[33], based on S transform, requires a sampling rate of 10 kHz and faults detection within 1.3ms but the method becomes less accurate when the fault resistance exceeds 14 Ω. Similarly, the HHT in[34] operates at 10 kHz with a fault detection time of 2ms but is limited to a fault resistance of 50 Ω. The discrete wavelet in[38] requires a higher sampling rate of 50 kHz and detect fault in 3ms, but it is restricted to lower fault resistance levels. In contrast, the method in[37] also based on discrete wavelet but utilizing a ratio of forward and backward traveling waves, fault detection in 3 ms at 10 kHz and can tolerate fault resistances up to 300 Ω. The modal domain analysis in[36] achieves a faster operation time of 1.1ms but has a fault resistance of 200Ω. Furthermore, the FFT in[39] has a short fault detection time of 0.5ms but requires a high sampling rate of 2 MHz.

The proposed protection method operates within 1 ms and can handle fault resistances up to 500Ω. These results highlight the benefits of the proposed method over previous existing methods, making it an effective and reliable solution for HVDC grid protection.

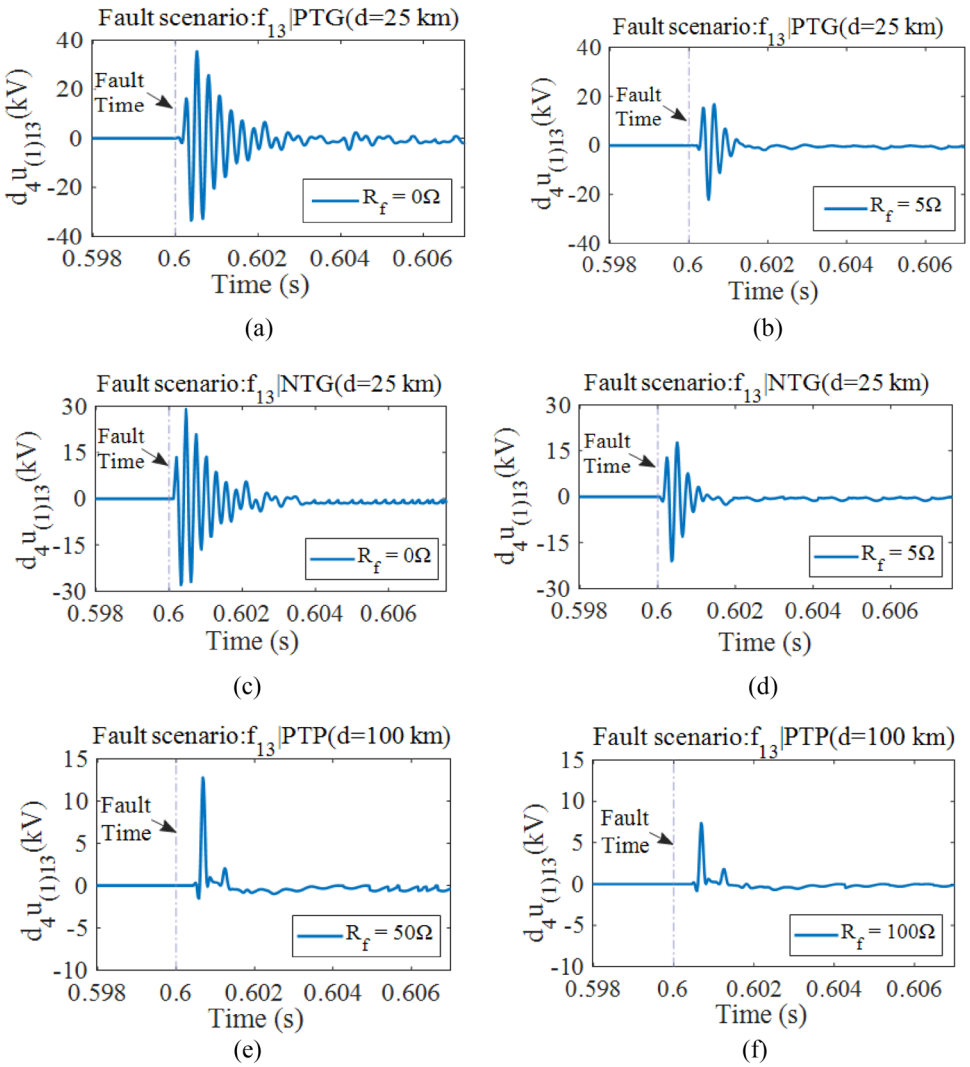

Fig. 9. Wavelet coefficients under fault scenarios.

Conclusion

The effective protection of DC cables is crucial for the continued development of large-scale VSC-HVDC gird systems. This study proposes an adaptive and robust non-unit traveling wave algorithm for HVDC multi-terminal systems. The wavelet discrete transform, incorporating the 'Daubechies' wavelet, is selected as a time-frequency signal-processing technique. The performance of the proposed algorithm has been rigorously evaluated in EMTDC/PSCAD using a four-terminal, five-cable meshed grid. The protection algorithm consists of four steps: First, the protection system activates once the DC voltage is less than 305.54 kV (0.95p.u.). Second, the fault area is determined by analyzing the fourth-level detailed coefficients of the voltage line mode traveling waves. Third, the injected traveling wave identifies the fault location. Fourth, identify the fault type by comparing the wavelet energy of the detailed components. Based on the obtained results, the proposed algorithm ensures efficient fault detection within 1 ms. The protection works properly under 25 dB of Gaussian noise interface. The protection reliably activates for all internal faults while remaining inactive for external faults like DC bus faults, and AC grid faults. The protection discriminates and detects various types of faults up to 500Ω. The results validate the protection algorithm will reduce the fault clearance times. The algorithm is highly accurate in detecting several types of faults (such as positive PTG, NTG, and PTP).

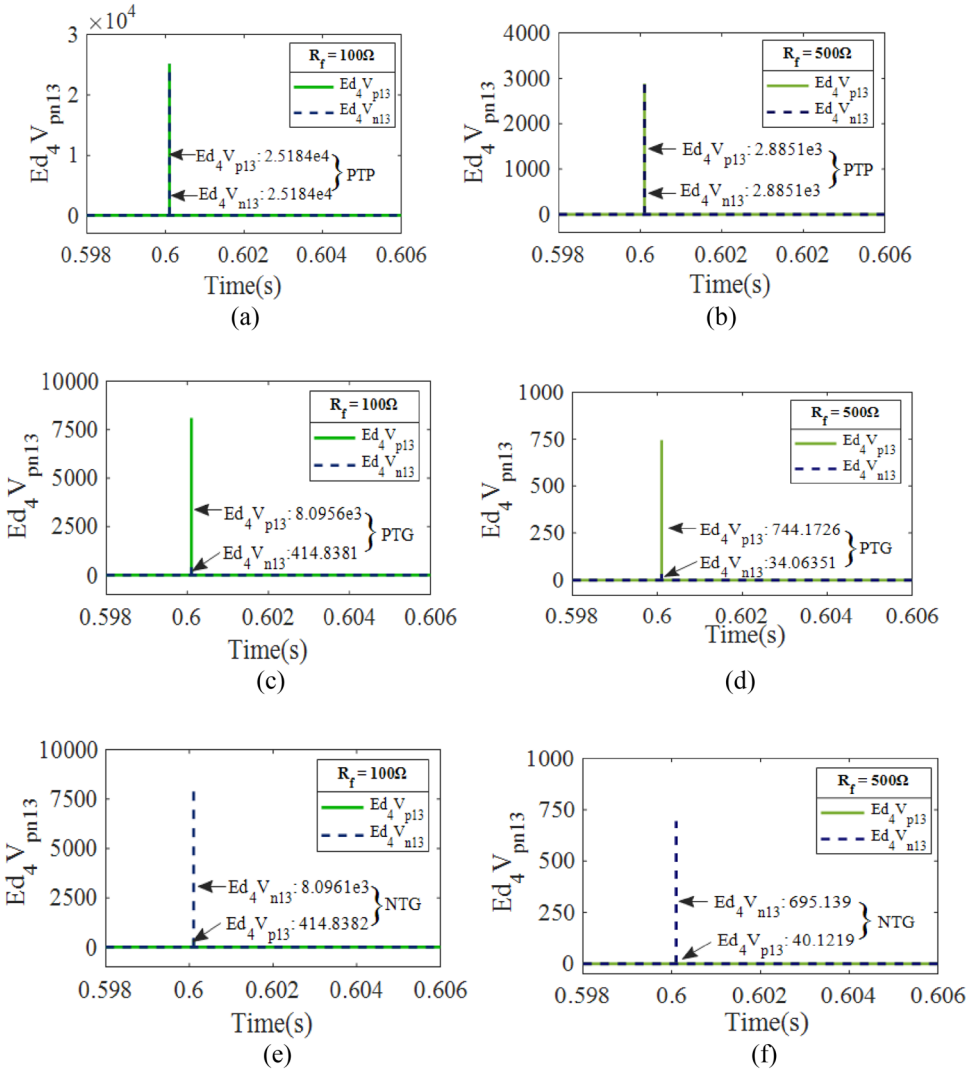

Fig. 10. Wavelet energy comparison of the positive and negative pole.

R_f (Ω)	$d_4u_{(1)13}$ (kV)	ΔE_{13} (kV)	Fault detection time (ms)
0	141.58	1.58e6	0.61
50	19.689	2.36e4	0.63
100	15.599	7.68e3	0.66
200	9.2521	2.34e3	0.72
300	6.2512	1.13e3	0.74
500	7.6624	7.10e2	0.88

Table 2. Results under fault condition: F_{13}|PTG (d = 25 km).

R_f (Ω)	$d_4u_{(1)13}$ (kV)	ΔE_{13} (kV)	Fault detection time (ms)
0	141.58	-1.57e6	0.59
50	19.688	-2.36e4	0.64
100	15.599	-7.68e3	0.68
200	9.2521	-2.34e3	0.73
300	6.2512	-1.13e3	0.80
500	6.2559	-6.55e2	0.87

Table 3. Results under fault condition: F_{13}|NTG (d = 25 km).

R_f (Ω)	$d_4u_{(1)13}$ (kV)	ΔE_{13} (kV)	Fault detection time (ms)
0	190.23	1.35e-6	0.61
50	76.76	1.21e-7	0.65
100	41.83	1.48e-7	0.69
200	23.38	1.84e-8	0.72
300	22.96	3.69e-8	0.75
500	13.47	7.13e-8	0.76

Table 4. Results under fault condition: F_{13}|PTP (d = 100 km).

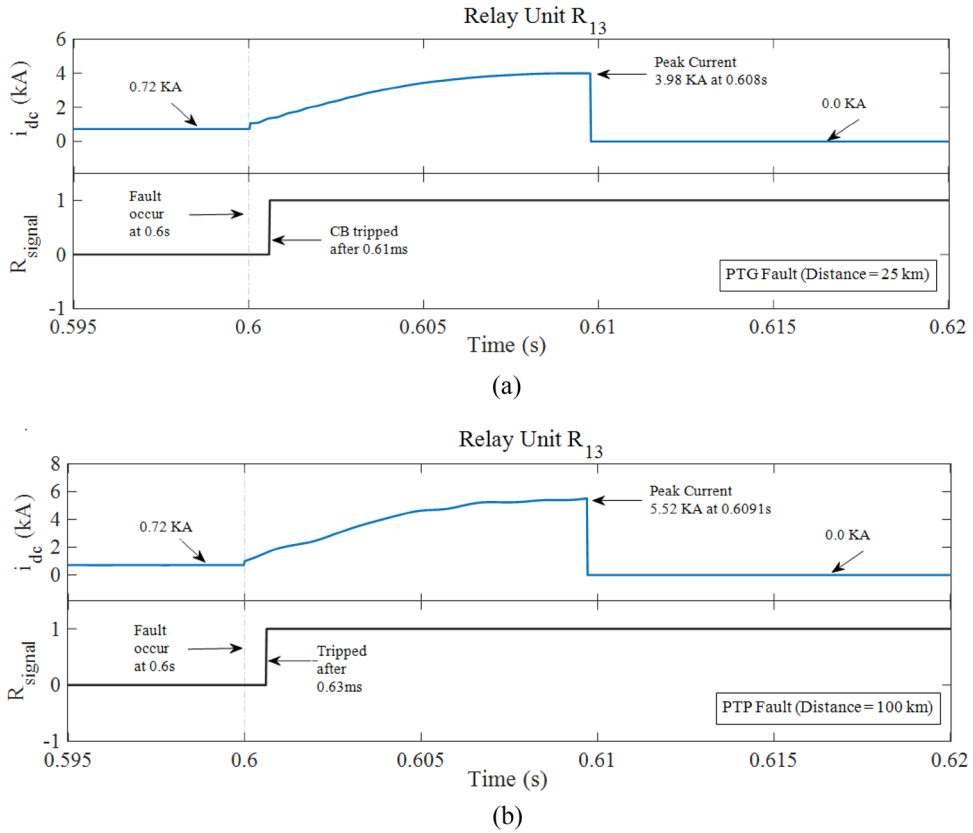

Fig. 11. VARC DCCB fault current interruption (a) f_{13}|PTG (d = 25 km, R_f = 0Ω). (b) f_{13}|PTP (d = 100 km, R_f = 5Ω).

External fault	R_f (Ω)	$d_4u_{(1)13}$ (kV)	ΔE_{13} (kV)	Detection step 2
f_2 |(DC Bus 1)	0.01	3.99	7.5e-9	×
f_1 |(DC Bus 2)	0.50	2.23	1.3e-8	×
f_3 |(DC Bus 3)	0.70	1.41	7.1e-8	×
f_4 |(DC Bus 4)	0.90	0.16	3.4e-6	×

Table 5. Results under external condition.

External cable (d = km, R_f = Ω)	$d_4u_{(1)13}$ (kV)	ΔE_{13} (kV)	Detection
f_{12}|PTG (d = 25, R_f = 0)	0.169	2.9e-6	×
f_{24}|PTP (d = 25, R_f = 50)	0.151	3.7e-6	×
f_{34}|NTG (d = 25, R_f = 100)	0.085	2.2e-7	×
f_{14}|PTP (d = 100, R_f = 200)	0.019	5.2e-9	×
f_{34}|PTG (d = 100, R_f = 300)	0.011	3.9e-6	×
f_{24}|NTG (d = 100, R_f = 500)	0.009	4.1e-8	×

Table 6. Results of protection for non-faulted cable.

Fault type	SNR	Rf Ω	$d_4u_{(1)13}$	ΔE_{13}	Fault detection
f_{13}| PTG (d = 25 km)	25 dB	0	173.8	1.51e6	✓
		50	87.04	1.41e4	✓
	50 dB	100	16.48	7.63e3	✓
		200	9.480	2.35e3	✓
	75 dB	300	6.359	1.13e3	✓
		500	4.096	4.38e2	✓
f_{13}| NTG (d = 25 km)	25 dB	0	129.1	-1.61e6	✓
		50	90.96	-2.23e4	✓
	50 dB	100	18.93	-7.86e3	✓
		200	12.27	-2.16e3	✓
	75 dB	300	6.187	-1.13e3	✓
		500	5.545	-6.73e2	✓

Table 7. Results under different noise levels and fault resistance.

Reference	Signal processing technique	Fault detection criterion	Tested grid system	Fault detection time	Fault resistance	Sampling rate
[33]	S Transform	Gaussian	Meshed seven terminal grid	1.3 ms	2 Ω to 14 Ω	10 kHz
[34]	Hilbert Huang	Instantaneous energy density level	Meshed seven terminal grid	2 ms	50 Ω	10 kHz
[37]	Discrete Wavelet	Backward & Forward TW ratio	Three terminal grid system	3ms	300Ω	10 kHz
[36]	Modal Domain analysis	Line mode reactor voltage	Meshed four terminal grid	1.1 ms	200Ω	100 kHz
[35]	Hilbert Huang	Average frequency	Meshed four terminal grid	4 ms	1Ω	25 kHz
[38]	Discrete Wavelet	Wavelet energy	Three terminal star-connected grid	3 ms	50Ω	50 kHz
[39]	Fast Fourier Transform	TW frequency spectral ratio	CIGRE grid model	0.5 ms	200Ω	2 MHz
Proposed technique	Daubechies wavelets transform	Energy of wavelet coefficients	Four terminals with five cables meshed grid	1 ms	500Ω	50 kHz

Table 8. Comparison between existing and proposed protection techniques.

Data availability

The data used to support the findings of this study are available from the corresponding author upon request.

Received: 14 July 2025; Accepted: 9 September 2025
Published online: 10 October 2025

References

1. Li, Y. et al. Direction protection based on Time-domain travelling wave for flexible MTDC grid. *CSEE J. Power Energy Syst.* **9**, 1414–1424 (2023).
2. Pragati, A. et al. A comprehensive survey of HVDC protection system: fault analysis, methodology, issues, challenges, and future perspective. *Energies* **16**, 7 (2023).
3. Guo, Z., Zhao, R., Li, H. & Jiang, Y. Transient voltage unit protection based on fault information fusion. *IEEE Access* **12**, 184583–184591 (2024).
4. Li, Y. et al. A novel non-unit traveling-wave protection method for parallel multi-terminal HVDC systems. *CSEE J. Power Energy Syst Early Access.*. https://doi.org/10.17775/CSEEJPES.2023.02540 (2023).
5. Han, K., Chen, Y., We, M. & Ma, R. A novel pilot protection scheme based on differential voltage for hybrid LCC/MMC HVDC transmission lines. *IEEE Trans. Power Deliv.*. **39** (3), 1816–1826 (2024).
6. Xiao, H., Li, Y. & S. R,en and Novel disturbance blocking criterion for reliable current differential protection of LCC-HVDC lines. *IEEE Trans. Power Deliv.* **36** (1), 477–480 (2021).
7. Tourn, D. H. et al. Signal processing for high impedance differential protection schemes. *IEEE Trans. Ind. Appl.* **60**, 7702–7710 (2024).
8. Liu, L., Lekić, A. & Popov, M. Robust traveling wave-based protection scheme for multiterminal DC grids. *IEEE Trans. Power Deliv.* **38**, 3117–3129 (2023).
9. Li, B., Li, Y., He, J. & Wen, W. A novel single-ended transient-voltage-based protection strategy for flexible DC Grid. *IEEE Trans. Power Deliv.* **34**, 1925–1937 (2019).
10. Naidu, O. D., George, N., Zubic, S. & Krakowski, M. Time-domain-based distance protection for transmission networks: secure and reliable solution for complex networks. *IEEE Access* **11**, 104656–104675 (2023).
11. Quispe, J. C. et al. Time-frequency multiresolution of fault-generated transient signals in transmission lines using a morphological filter. *Prot. Control Mod. Power Syst.* **8**, 1–14 (2023).
12. Li, C., Go, A. M. & Zhao, C. A fast DC fault detection method Using DC reactor voltages in HVdc Grids. *IEEE Trans. Power Deliv.* **33**, 2254–2264 (2018).
13. Xiang, W. et al. Dc fault protection algorithms of mmc-hvdc grids: fault analysis, methodologies, experimental validations, and future trends. *IEEE Trans. Power Electron.* **36** (10), 245–11264 (2021).
14. Li, R., Xu, L. & Yao, L. Dc fault detection and location in meshed multiterminal Hvdc systems based on Dc reactor voltage change rate. *IEEE Trans. Power Deliv.* **32**, 1516–1526 (2017).
15. Pérez Molina, M. J., Escobal, D. M. L., Lopez, P. E. & Valverde Santiago, V. Fault detection based on ROCOV and ROCOC for multi-terminal HVDC systems. In *2020 IEEE 20th Mediterranean Electrotechnical Conference (MELECON), Palermo, Italy* (2020).
16. Pérez-Molina, M. J., Larruskain, D. M., Eguía, P. & Santiago, V. V. Local derivative-based fault detection for HVDC grids. *IEEE Trans. Ind. Appl.* **58**, 1521–1530 (2022).
17. Raghpoor, V., Mehrabi-Kooshki, M. & Razzaghi, R. A novel non-unit protection scheme for HVDC transmission lines based on multi-resolution morphology gradient, *M.S. thesis, Monash Univ.*, Melbourne, Australia (2021).
18. Dashtdar, M. et al. Protection of DC microgrids based on frequency domain analysis using Fourier transform. In *Proc. IEEE 3rd KhPI Week on Advanced Technology (KhPIWeek), Kharkiv, Ukraine* 1–6 (2022).
19. Kaur, J. et al. Fault detection and protection strategy for multi-terminal HVDC grids using wavelet analysis. *Energies* **18**, 1147 (2025).

20. Li, D., Ukil, A., Satpathi, K. & Yeap, Y. M. Hilbert–Huang transform based transient analysis in voltage Source converter interfaced direct current system. *IEEE Trans. Ind. Electron.* **68**, 11014–11025 (2021).
21. Ahmadi-khaneghahi, Y., Shahabi, M., Barforoushi, T. & Ahmadi, I. A fast and robust local-based protection algorithm based on the high-frequency transient for HVDC grid. *IEEE Trans. Power Deliv.* **38**, 2531–2540 (2023).
22. Grcic, H., Pandzic & Novosel, D. Fault detection in DC microgrids using short-time Fourier transform. *Energies* **14**, 277 (2021).
23. de Souza, U. B., Escola, J. P. L. & Brito, L. A survey on Hilbert-Huang transform: evolution, challenges and solutions. *Digit. Signal Process* **120**, 103292 (2022).
24. Wang, Y. et al. An adaptive high-voltage direct current detection algorithm using cognitive wavelet transform. *Inf. Process. Manag* **59**, 102867 (2022).
25. Li, B. et al. An improved transient traveling-wave based direction criterion for multi-terminal Hvdc grid. *IEEE Trans. Power Deliv.* **35**, 2517– 2529 (2020).
26. Ghazizadeh, M., Ajaei, F. B. & Dounavis, A. Passive lumped DC line model with frequency-dependent parameters for transient studies. *IEEE Trans. Power Deliv.* **37**, 3947–3957 (2022).
27. Rosyadi, M. et al. A simplified model design of MMC-HVDC transmission system for steady state and transient stability analyses. *Int. J. Power Electron. Drive Syst.* **14**, 934–947 (2023).
28. Haider, A., Ahmed, N., Ängquist, L. & Nee, H. P. Open-loop approach for control of multi-terminal DC systems based on modular multilevel converters. In *Proceedings of the 2011 14th European Conference on Power Electronics and Applications, Birmingham, UK* 1–9 (2011).
29. Zhang, C., Song, G., Wang, T., Wu, L. & Yang, L. Non-unit Traveling Wave Protection of HVDC grids using Levenberg–Marquart optimal approximation. *IEEE Trans. Power Deliv.* **35**, 2260–2271 (2020).
30. Guo, T. et al. A review of wavelet analysis and its applications: challenges and opportunities. *IEEE Access.*, **10**, 58869–58903 (2022).
31. Jahn, F., Hohn, G., Chaffey & Norrga, S. An Open-Source protection IED for research and education in multiterminal HVDC grids. *IEEE Trans. Power Syst.* **35** (4), 2949–2958 (2020).
32. Katoulaei, M. K. et al. Backup subscription scheme for differential protection using IEC61850-9-2 sampled values. *Energy Inf.* **7**, 110 (2024).
33. Li, D., Ukil, A., Satpathi, K. & Yeap, Y. M. Improved s transform-based fault detection method in voltage source converter interfaced DC system. *IEEE Trans. Ind. Electron.* **68**, 5024–5035, (2021).
34. Li, D., Ukil, A., Satpathi, K. & Yeap, Y. M. Hilbert–Huang transform based transient analysis in voltage source converter interfaced direct current system. *IEEE Trans. Ind. Electron.* **68**, 11014–11025 (2021).
35. Lacerda, V. A., Monaro, R. M., Campos-Gaona, D., Coury, D. V. & Anaya-Lara, O. Distance protection algorithm for multiterminal HVDC systems using the Hilbert–Huang transform. *IET Gener. Transm. Distrib.* **14** (15), 3022–3032 (2020).
36. Yang, S. et al. An improved DC fault protection algorithm for MMC HVDC grids based on modal-domain analysis. *IEEE Trans. Emerg. Sel. Topics Power Electron.* **8**, 4086–4099 (2020).
37. Li, B. et al. An improved transient traveling-wave based direction criterion for multi-terminal HVDC grid. *IEEE Trans. Power Deliv.* **35**, 2517–2529 (2020).
38. Mitra, B., Chowdhury, B. & Willis, A. Protection coordination for assembly HVDC breakers for HVDC multiterminal grids using wavelet transform. *IEEE Syst. J.* **14** (1), 1069–1079 (2020).
39. Saleh, K. A., Hooshyar, A., El Saadany , E. F., & Zeineldin, H. H. Protection of high-voltage DC grids using traveling wave frequency characteristics. *IEEE Syst. J.* **14**, 4284–4295 (2020).

Author contributions

AR, MAH, ARK, MZY, BK, JMG and RS wrote the main manuscript text. AR, MAH, ARK, MZY, BK, JMG and RS prepared figures. All authors reviewed the manuscript.

Funding

There is no funding available for this research in any form.

Competing interests

The authors declare no competing interests.

Additional information

Correspondence and requests for materials should be addressed to M.Z.Y., B.K. or R.S.

Reprints and permissions information is available at www.nature.com/reprints.

Publisher's note Springer Nature remains neutral with regard to jurisdictional claims in published maps and institutional affiliations.